INTERNATIONAL JOURNAL FOR NUMERICAL METHODS IN FLUIDS, VOL. 11, 985–1000 (1990)

TRANSIENT FLOW PAST A CIRCULAR CYLINDER: A BENCHMARK SOLUTION

MICHAEL S. ENGELMAN AND MOHAMMAD-ALI JAMNIA
Fluid Dynamics International, Evanston, IL 60201, U.S.A.

SUMMARY

The simulation of the von Karman vortex street behind a circular cylinder has long been used as a benchmark problem to test the performance of numerical algorithms for solving the Navier–Stokes equations. It is particularly suited for comparing different numerical outflow boundary conditions since the computational domain must necessarily be terminated in the vortex street itself. This paper presents detailed numerical results of the flow past a cylinder at a Reynolds number of 100 on a very fine mesh which has been purposely designed to extend past the typically used dimensions. Hopefully, these results can form a basis of a benchmark solution for the comparison of the effects of different outflow boundary conditions.

KEY WORDS Outflow boundary conditions Vortex shedding Finite element method

INTRODUCTION

The simulation of the von Karman vortex street behind a circular cylinder has been addressed by numerous authors using a wide range of numerical methods. The purpose of the study reported herein is to provide a benchmark solution for this problem which can provide a basis for comparison of outflow boundary conditions. This problem is a particularly challenging one for an outflow boundary condition since the computational domain must be terminated in an area where the vortex street is fully developed. The outflow boundary condition should be such that it allows the vortices to leave the computational domain while not disturbing the vortex shedding occurring upstream.

The problem considered here is the flow past a circular cylinder in a freestream at a Reynolds number of 100. Because only a finite computational domain can be employed for the numerical simulation, it is important to locate the inflow and far-field boundaries at sufficient distance such that the boundary conditions applied at these boundaries do not introduce significant effects into the main region of interest around and behind the cylinder. The inflow, top and bottom boundaries have been located eight cylinder diameters in front of, above and below the centre of the cylinder respectively. Similarly, in order to minimize the effects of the outflow boundary condition on the flow in the vicinity of the cylinder, the computational mesh has been extended 25·2 (the extra 0·2 is to accommodate the quadratic finite elements employed) cylinder diameters downstream of the centre of the cylinder.

The boundary conditions for the problem include an imposed value of 1·0 for the x-component of velocity at the inflow and at the top and bottom boundaries of the computational domain. At these boundaries the y-component of velocity was specified to be zero, i.e. tow tank boundary

0271–2091/90/150985–16$08.00

Received 21 May 1990
Revised 26 June 1990

conditions. The outflow boundary condition was the natural one that arises in the context of the finite element method applied to the Navier–Stokes equations. Since the $\nabla^2\mathbf{u}$ form of the diffusion term was employed rather than the stress–divergence form, this boundary condition takes the form

$$-P+\mu\frac{\partial u}{\partial x}=0, \qquad \mu\frac{\partial v}{\partial x}=0.$$

Note that this boundary condition is applied in a weak sense rather than in a pointwise manner.

The non-dimensional form of the Navier–Stokes equations was employed for the simulation. For an isothermal problem with a fixed geometry this results in the Reynolds number being the only non-dimensional parameter required; the Reynolds number is defined by $Re=DU/v$, where D is the diameter of the cylinder, U is the freestream velocity and v is the kinematic viscosity. Since both the diameter of the cylinder and the freestream velocity were set to unity, the kinematic viscosity was set to 0·01 to achieve the desired Reynolds number.

NUMERICAL METHOD

The numerical simulation described in this paper was performed using the FIDAP programme,[1] a general purpose programme for the simulation of incompressible flows which is based on a Galerkin finite element formulation. A complete description of the numerical techniques employed can be found in Reference 1—only a brief overview of the particular approach employed for this simulation will be presented here. The primitive variable form of the Navier–Stokes equations was employed with a penalty function approach for the pressure. Nine-node quadrilateral finite elements were used with a biquadratic Lagrange interpolation function for the velocity and a linear polynomial approximation for the pressure; thus the velocity approximation is continuous between elements while the pressure approximation is discontinuous. The penalty approach was implemented using the consistent matrix approach described in Reference 2. The value of the penalty parameter was 10^{-7}.

The transient time integration was performed using an implicit predictor–corrector finite difference scheme. The corrector step used the second-order-accurate and non-dissipative trapezoid rule while the predictor step was an Adams–Bashforth scheme. For efficiency and accuracy a variable-time-increment approach was employed with the time increment at each time step being determined by controlling the local time truncation error at each step. Complete details of the time integration scheme can be found in References 1 and 3. The local time truncation error tolerance used for the simulation was 0·0005, i.e. the local time truncation error between time steps was allowed to be no greater than 0·05%—a fairly tight tolerance.

Because an implicit time integrator was used, a non-linear system of algebraic equations must be solved at each time step. A quasi-Newton non-linear iterative solver was used to solve this non-linear system (see Reference 4 for details on the quasi-Newton solver). This approach is more cost-effective than a full Newton–Raphson strategy since it requires the formation of only one Jacobian matrix (and the associated system of linear equations) per time step. Also, because a predictor–corrector scheme is being used, if the specified local time truncation error tolerance is small, then the predictor is sufficiently accurate that only a few iterations of the non-linear iterative solver are typically required. For the simulations described in this paper only one or at the most two iterations were required to obtain convergence at each time step. A convergence tolerance of 0·01% on the normalized change in the solution vectors and a 0·01% change in the normalized residual vector was used to terminate the non-linear iteration scheme at each time

step. The non-symmetric linear equation system that had to be solved at each time step was solved using Gaussian elimination with a profile (skyline) storage scheme.[5]

In addition to the primary velocity and pressure variables, a number of derived quantities were computed as part of the benchmark solution. The streamfunction was computed from a line integral of the velocity components taken between nodal points along elements edges—a procedure described in detail in Reference 1. All other derived quantities, e.g. vorticity, stresses, etc., required the computation of derivatives of the computed velocity solution. These derivatives were computed using the element polynomial basis functions in the usual manner. In order to maximize the accuracy, wherever possible these derivatives were evaluated at the 2×2 points of Gaussian quadrature within the element; these computed values were then projected to the corner nodes of the element and an area-weighted average computed in order to obtain a continuous field. For plotting purposes, midside node data were linearly interpolated from corner node data.

COMPUTATIONAL MODELS

In an effort to demonstrate that the reported solutions are converged in the mesh refinement sense, computations were performed on three meshes of increasing refinement. For discussion purposes these meshes will be referred to as the coarse, medium and fine mesh respectively—specific details for each mesh are provided in Table I. It should be noted that the 'coarse' mesh used in this study was significantly finer than other meshes used in previously reported simulations of the vortex-shedding problem.[6, 7]

For mesh generation purposes the computational domain was divided into a number of distinct regions: A square region, $-4 \leqslant x \leqslant 4$, $-4 \leqslant y \leqslant 4$, surrounding the cylinder; the regions upstream and downstream from this region; and the regions above and below the square region. The square region was meshed using a radial-type mesh graded inwards toward the cylinder with an average grading factor of 15, i.e. the ratio of the first element width to the last element width on a radial line segment was 15 (see Figure 1). The distance of the first node on the centreline downstream of the cylinder was 0·0359, 0·0196 and 0·0160 for the coarse, medium and fine meshes respectively. From $x=4$ to $x=25{\cdot}2$ the mesh was uniformly distributed. From $y=4$ to $y=8$ and from $y=-4$ to $y=-8$ the mesh was graded with a grading factor of two. The mesh was similarly graded from $x=-4$ to the inflow at $x=-8$ with a grading factor of two. The computational meshes are shown in Figure 1.

Since the ultimate purpose of this benchmark solution is to provide data for comparison of the efficacy of different numerical outflow boundary conditions, an additional mesh was generated. This mesh is identical to the fine mesh described above except that the computational domain and mesh is terminated at $x=4$; this will be referred to as the short mesh. This mesh may be considered as a means of evaluating the performance of the natural boundary conditions employed in this paper rather than as part of the benchmark solution.

Table I. Mesh characteristics

Mesh	Number of nodes	Number of elements	Width of first node	Number of equations
Coarse	6878	1672	0·0359	13090
Medium	9716	2376	0·0196	18694
Fine	14000	3436	0·0160	27102
Short	7110	1740	0·0160	13746

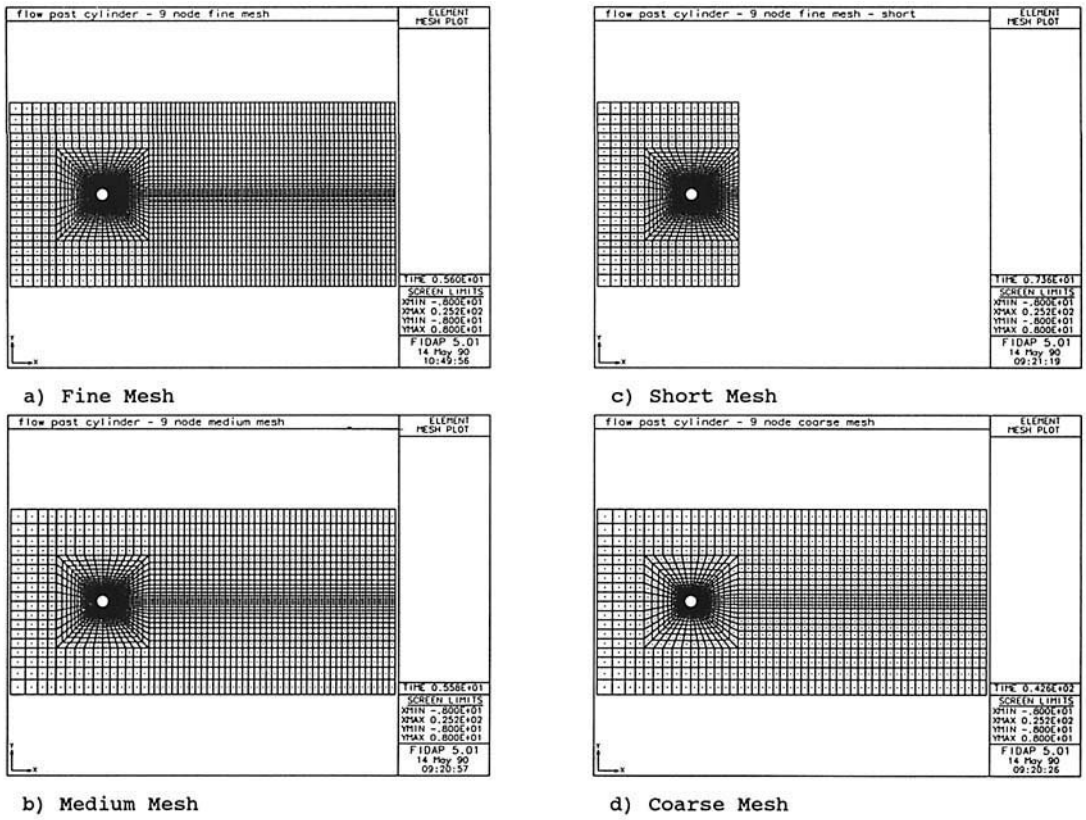

Figure 1. Different finite element meshes

In order to reach the vortex-shedding regime, the following sequence of simulations was performed. First a steady state simulation was performed on the coarse mesh. This solution was then used as the initial flow field for a transient simulation of 150 time steps. Vortices began to shed after approximately 50 time steps and by time step 150 the periodic vortex street was well established. The variable time increment settled down to a constant increment of 0·269 after 100 time steps. The flow field at time step 150 was then interpolated onto the medium and fine meshes and a transient simulation of 175 time steps performed for each of the three meshes (the simulation for the coarse mesh was simply restarted from the previous run). The results at the final time step of the fine mesh simulation were used on the truncated short mesh as the initial solution and a transient simulation of 175 time steps was performed. Each shedding cycle on the fine mesh required 22 times steps—time steps 25–175 were used for the results presented in this study. The time increment for these time steps was 0·269, 0·264, 0·266 and 0·3344 for the coarse, medium, fine and short meshes respectively.

RESULTS

The results are presented in Figures 2–21. Figures 2–5 are time history plots of the x-component of velocity, y-component of velocity, pressure and vorticity respectively. The time histories at four

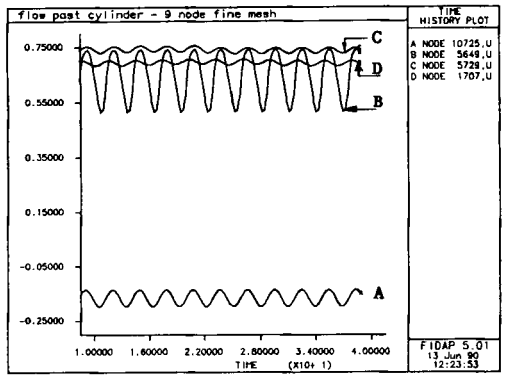

a) Fine Mesh

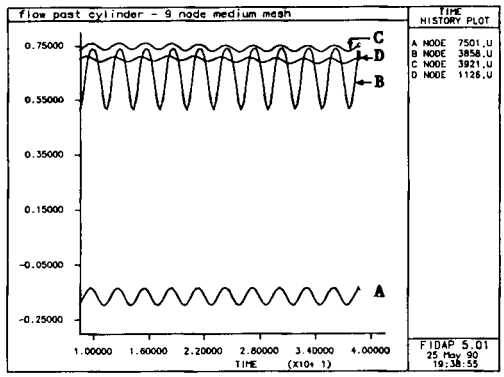

b) Medium Mesh

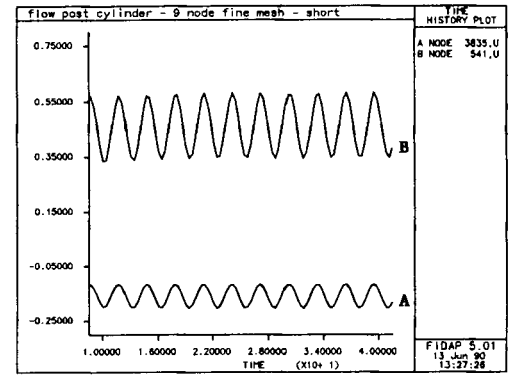

c) Short Mesh

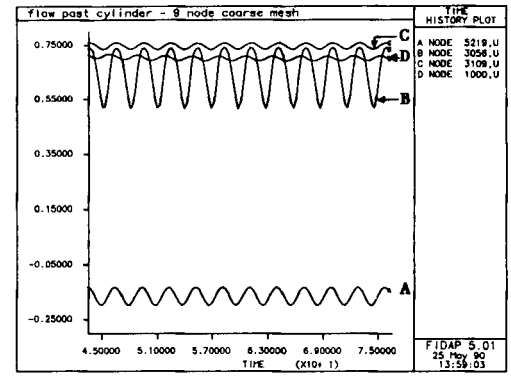

d) Coarse Mesh

Figure 2. Time history of u_x at $y=0$, $x=1$ (a), 4 (b), 20 (c) and 25·2 (d)

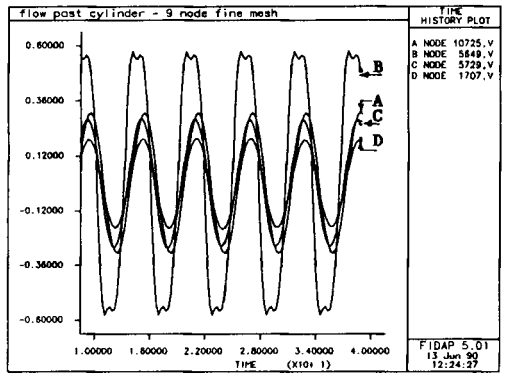

a) Fine Mesh

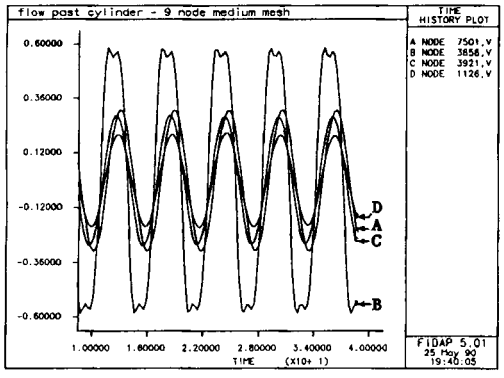

b) Medium Mesh

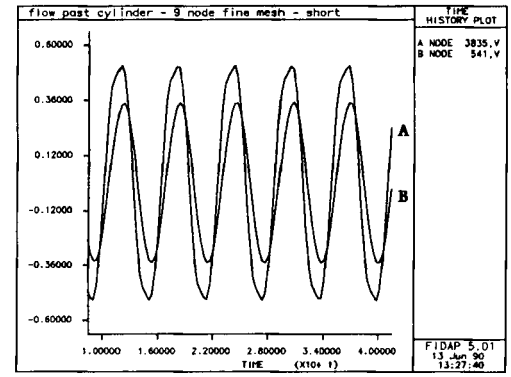

c) Short Mesh

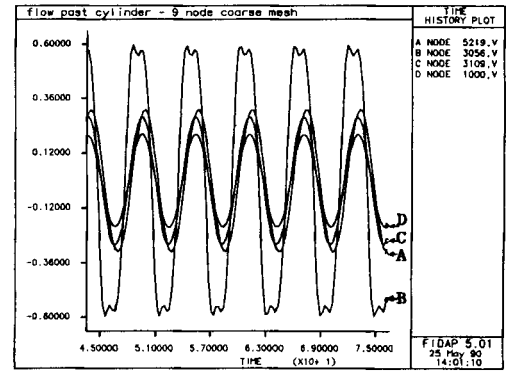

d) Coarse Mesh

Figure 3. Time history of u_y at $y=0$, $x=1$ (a), 4 (b), 20 (c) and 25·2 (d)

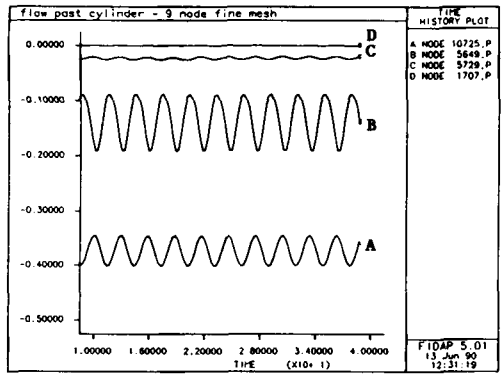

a) Fine Mesh

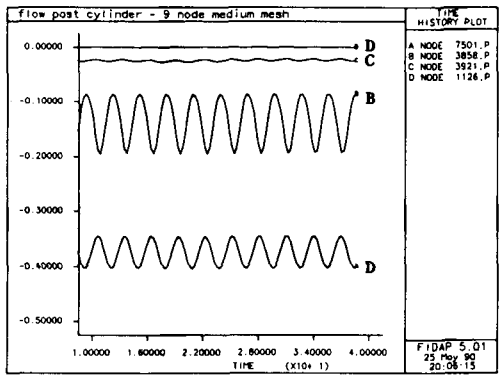

b) Medium Mesh

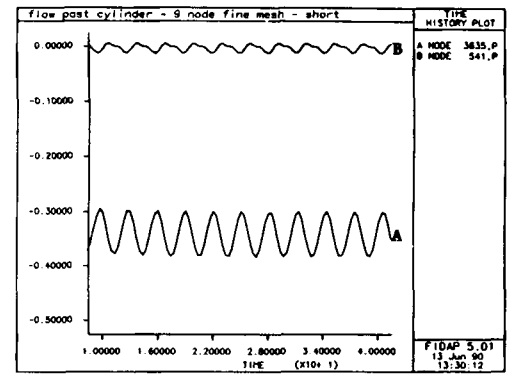

c) Short Mesh

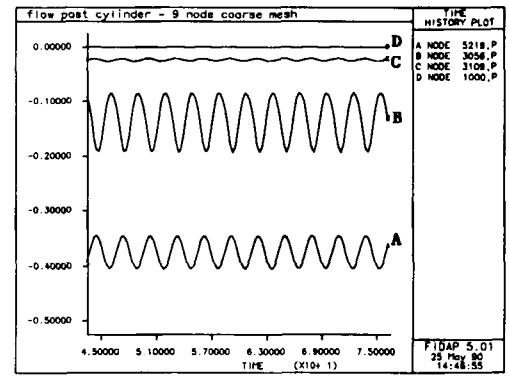

d) Coarse Mesh

Figure 4. Time history of pressure at $y=0$, $x=1$(a), 4(b), 20(c) and 25·2(d)

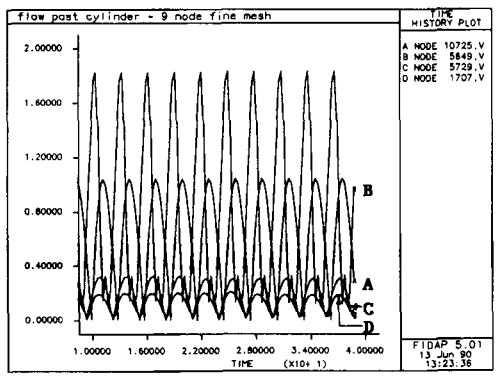

a) Fine Mesh

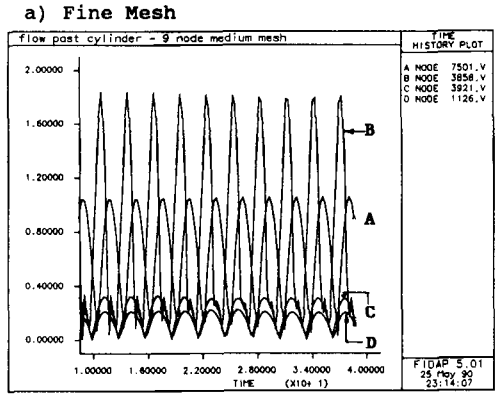

b) Medium Mesh

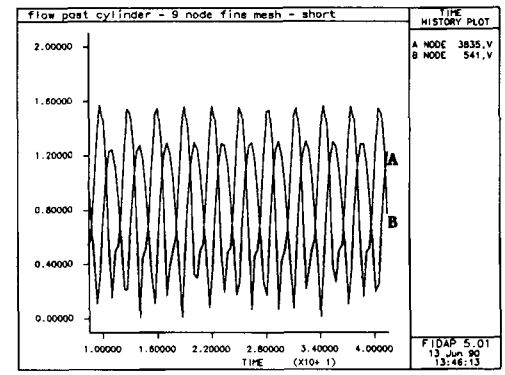

c) Short Mesh

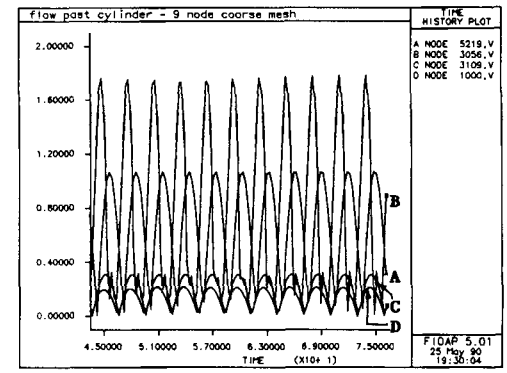

d) Coarse Mesh

Figure 5. Time history of vorticity at $y=0$, $x=1$(a), 4(b), 20(c) and 25·2(d)

locations on the centreline ($y=0$) are reported: $x=1$, 4, 20 and 25·2 (the outflow)—these points are labelled A, B, C and D respectively on the time history plots. Time histories of the drag and lift coefficients are shown in Figures 6 and 7 respectively for each of the meshes. The start-up effect of using the fine mesh result to restart the short mesh simulation is clearly evident in the drag history plot.

All the other results are the values of various quantities at a particular instant in the shedding cycle. By prior agreement this time, t_{ref}, was chosen to be the instant when the y-component of velocity was changing from a negative value to a positive value (i.e. passing through zero from below) at the point $x=4$ on the centreline. This time was determined for each mesh using the appropriate time history plot. As a time step did not exactly coincide with this time for any of the meshes, the solution at this time was interpolated using linear interpolation between the two bracketing time step solutions. For accuracy, this time was selected in the last full shedding cycle.

In order to provide data for the evaluation of various boundary conditions, cross-channel profiles of a variety of quantities are plotted at $x=4$ and 20 at the time t_{ref}. The quantities plotted are the x-component of velocity, y-component of velocity, $\partial u_x/\partial x$, $\partial u_y/\partial x$, $\partial u_x/\partial y$, $\partial u_y/\partial y$, normal stress ($-P+2\mu\partial u_x/\partial x$), tangential stress ($\mu(\partial u_x/\partial y+\partial u_y/\partial x)$), pressure and vorticity in Figures 8–15 for the fine and short meshes.

Figures 16–20 are contour plots (on the full domain) of the streamfunction, x-component of velocity, y-component of velocity, pressure and vorticity respectively at time t_{ref}. Figure 21 is a 'discrete dye plot'; this plot is the equivalent of flow visualization by the injection of dye into the flow stream. The dye was injected at the point (0·6, 0·75).

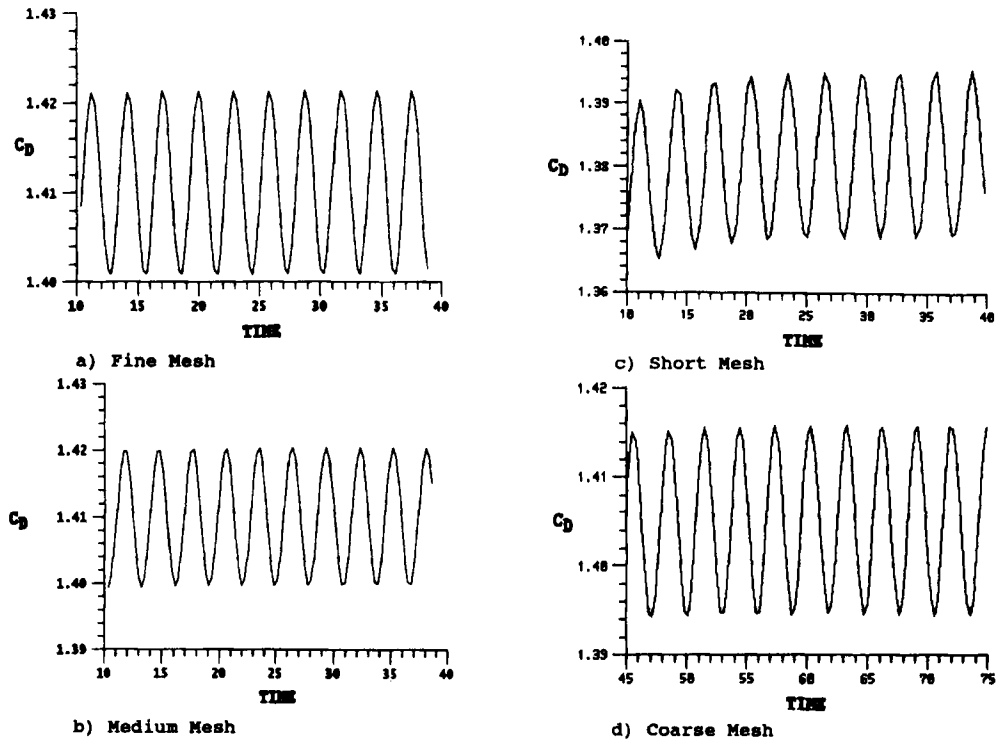

Figure 6. Comparison of drag coefficients for different meshes

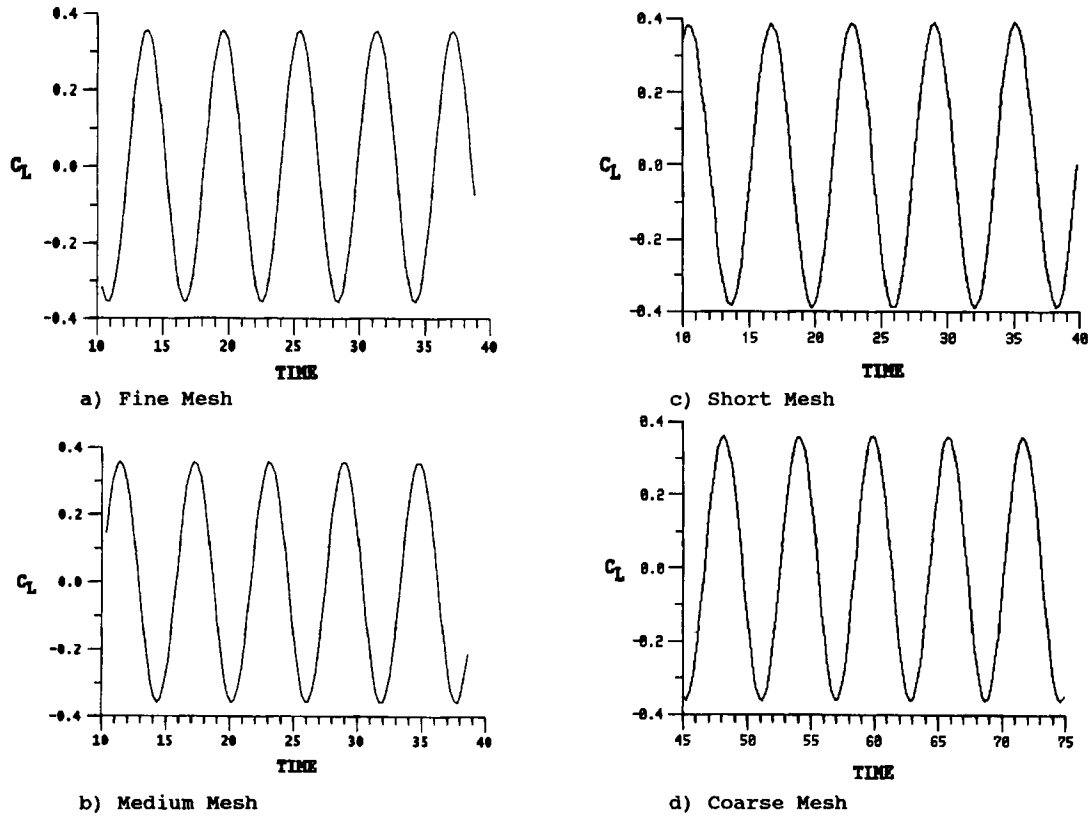

Figure 7. Comparison of lift coefficients for different meshes

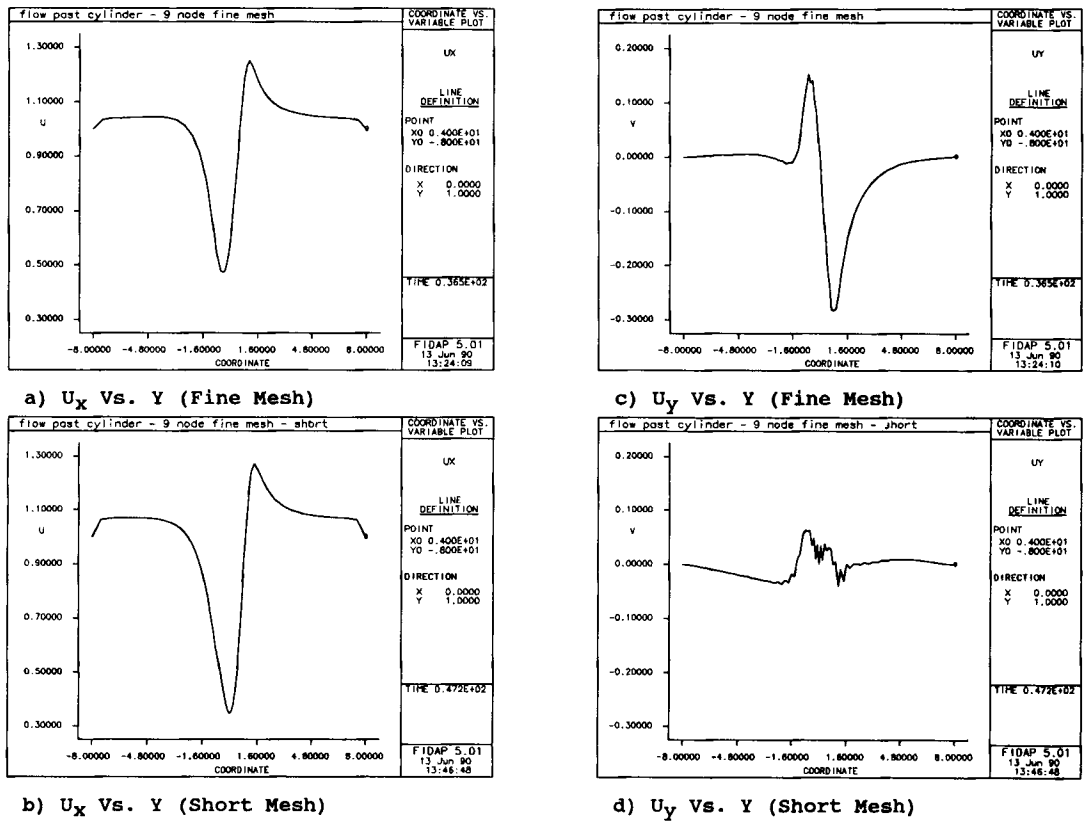

Figure 8. u_x and u_y at $x=4$ for fine and short meshes at t_{ref}

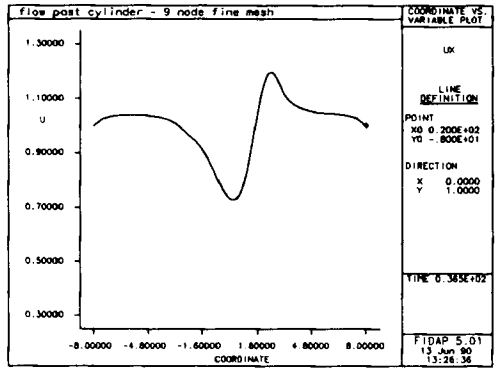

a) U_X Vs. Y (Fine Mesh)

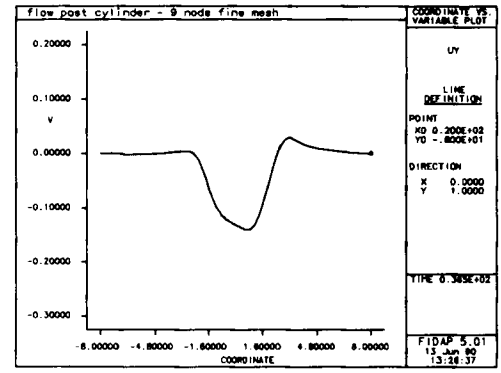

b) U_Y Vs. Y (Fine Mesh)

Figure 9. u_x and u_y at $x=20$ for the fine mesh at t_{ref}

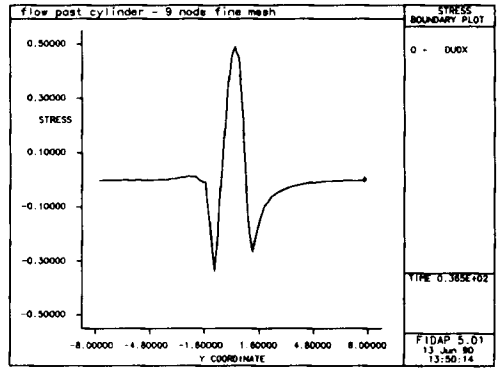

a) $U_{X,X}$ (Fine Mesh) Vs. Y

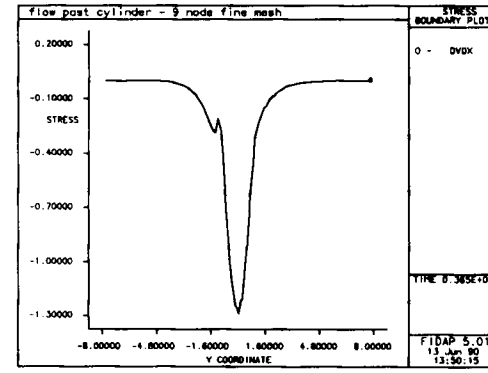

c) $U_{Y,X}$ (Fine Mesh) Vs. Y

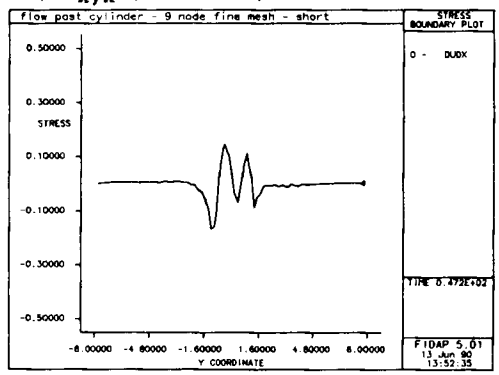

b) $U_{X,X}$ (Short Mesh) Vs. Y

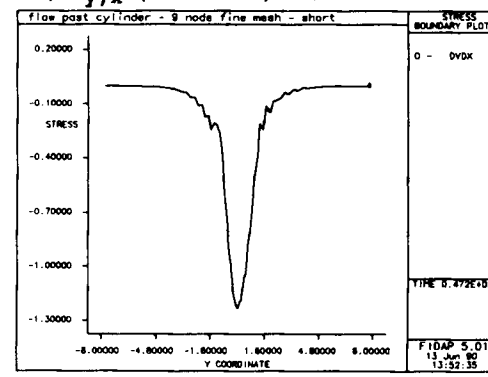

d) $U_{Y,X}$ (Short Mesh) Vs. Y

Figure 10. $u_{x,x}$ and $u_{y,x}$ evaluated at $x=4$ at t_{ref}

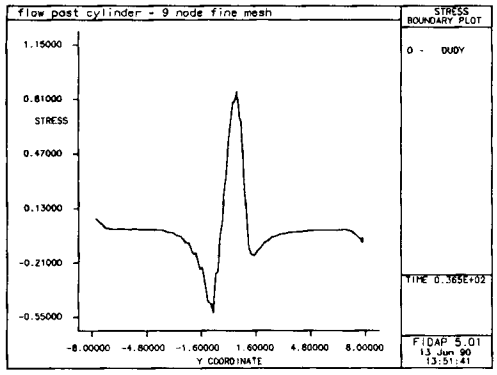

a) $U_{x,y}$ (Fine Mesh) Vs. Y

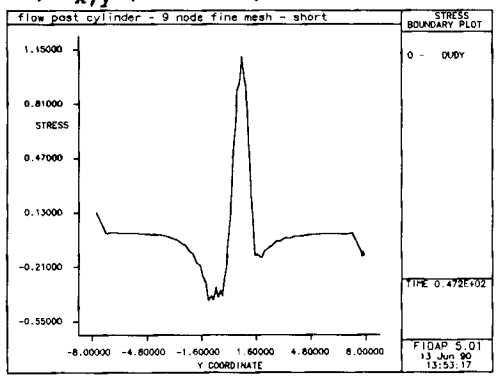

b) $U_{x,y}$ (Short Mesh) Vs. Y

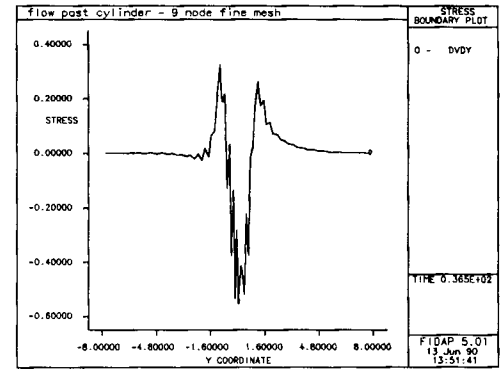

c) $U_{y,y}$ (Fine Mesh) Vs. Y

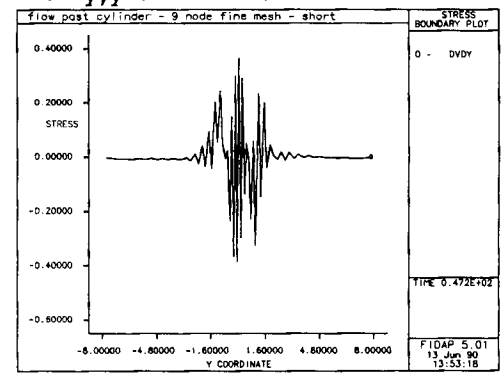

d) $U_{y,y}$ (Short Mesh) Vs. Y

Figure 11. $u_{x,y}$ and $u_{y,y}$ evaluated at $x=4$ at t_{ref}

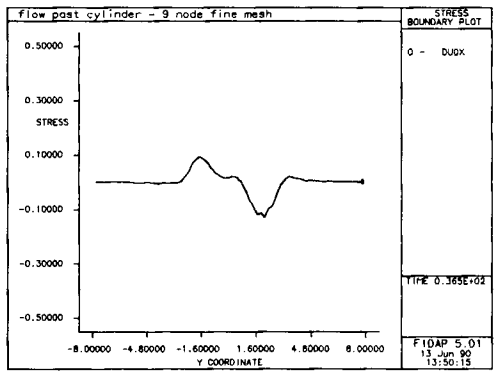

a) $U_{x,x}$ (Fine Mesh) Vs. Y

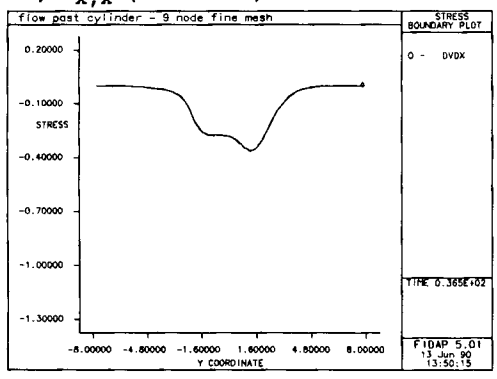

b) $U_{y,x}$ (Fine Mesh) Vs. Y

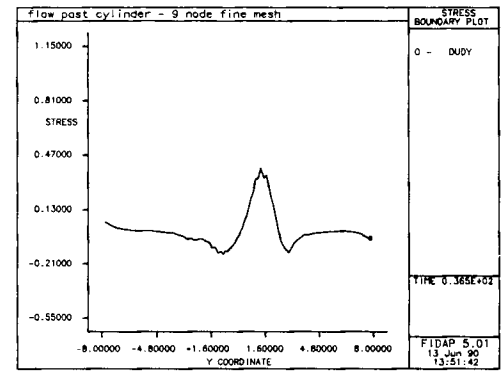

c) $U_{x,y}$ (Fine Mesh) Vs. Y

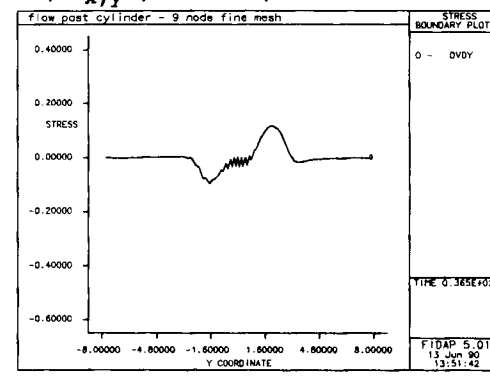

d) $U_{y,y}$ (Fine Mesh) Vs. Y

Figure 12. $u_{x,x}$, $u_{y,x}$, $u_{x,y}$ and $u_{y,y}$ evaluated at $x=20$ at t_{ref}

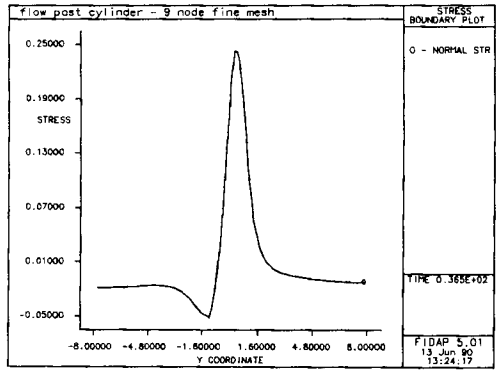

a) Normal Stress Plot (Fine Mesh)

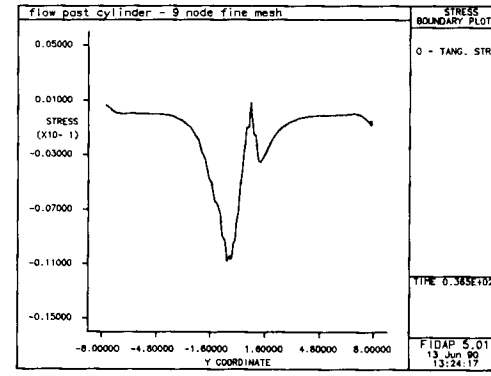

c) Tangential Stress Plot (Fine Mesh)

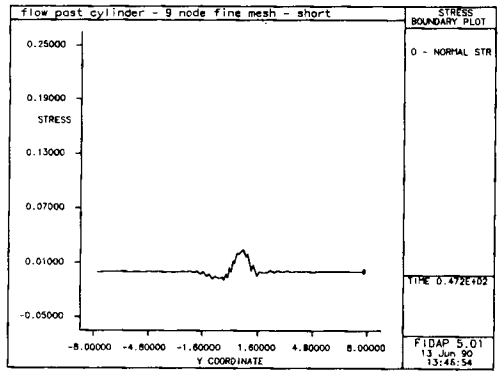

b) Normal Stress Plot (Short Mesh)

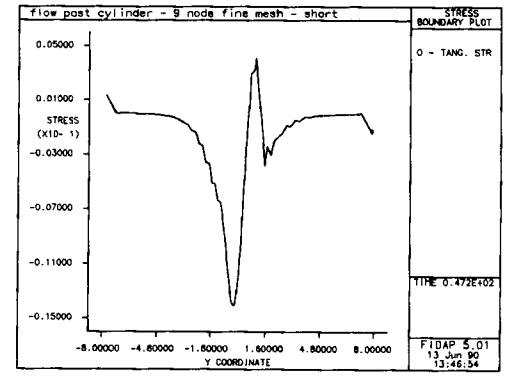

d) Tangential Stress Plot (Short Mesh)

Figure 13. Stresses at $x=4$ for fine and short meshes

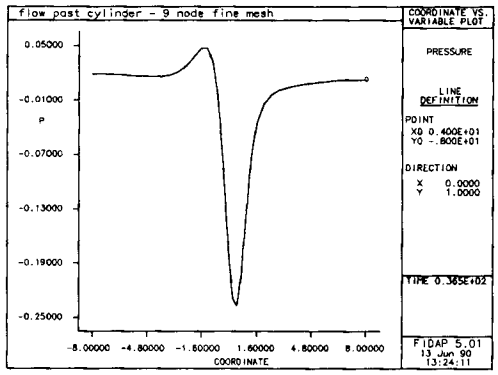

a) Pressure Distribution (Fine Mesh)

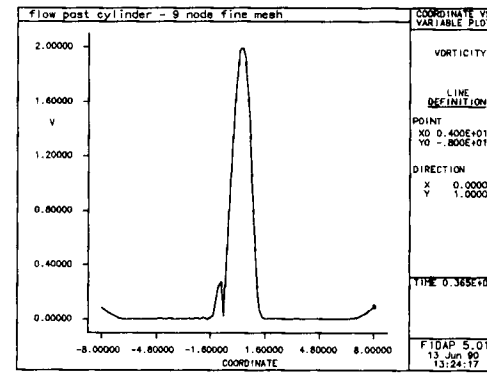

c) Vorticity (Fine Mesh)

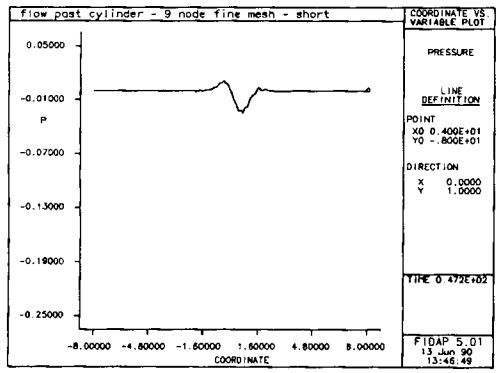

b) Pressure Distribution (Short Mesh)

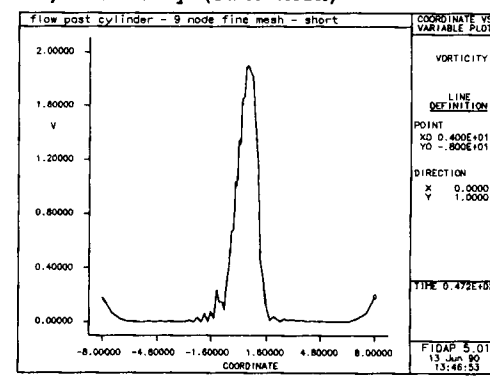

d) Vorticity (Short Mesh)

Figure 14. Pressure and vorticity at $x=4$ for fine and short meshes

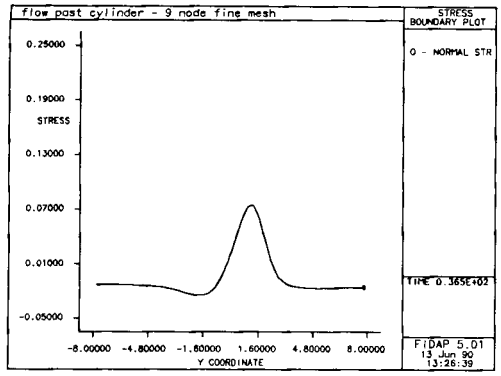

a) Normal Stresses (Fine Mesh)

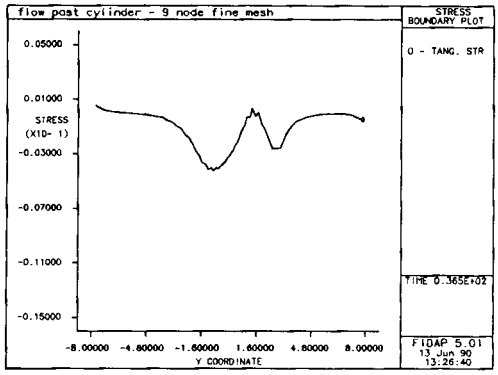

b) Tangential Stresses (Fine Mesh)

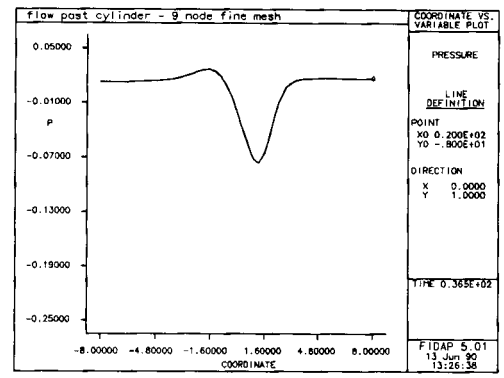

c) Pressure (Fine Mesh)

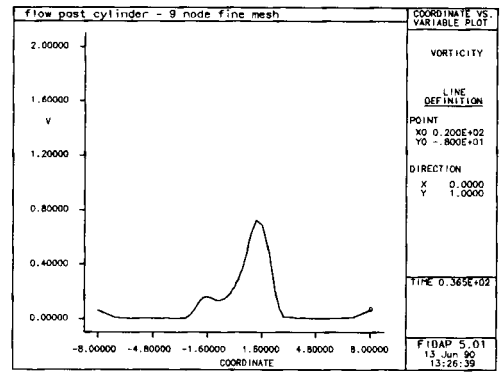

d) Vorticity (Fine Mesh)

Figure 15. Stresses, pressure and vorticity at $x=20$ for the fine mesh

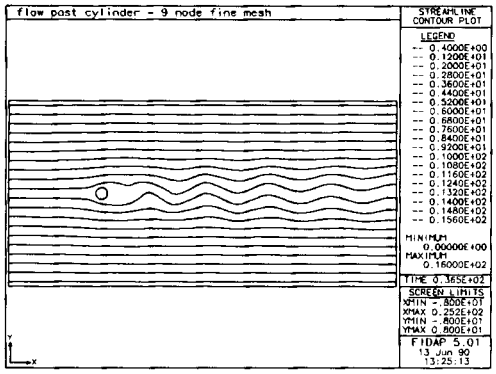

a) Fine Mesh

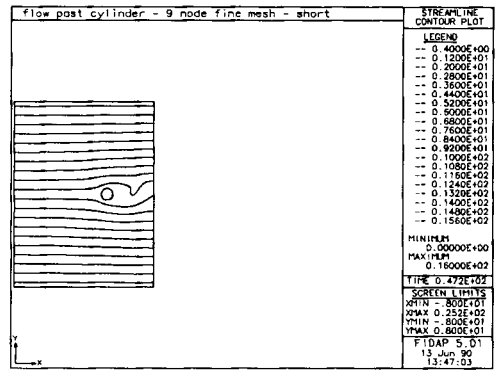

c) Short Mesh

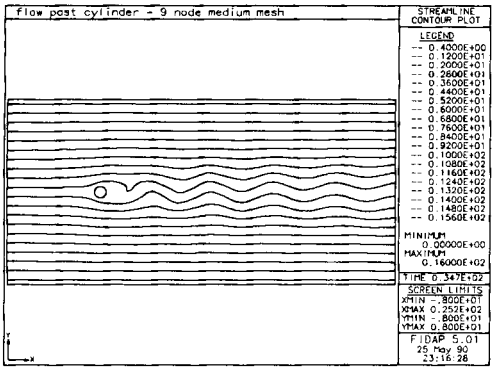

b) Medium Mesh

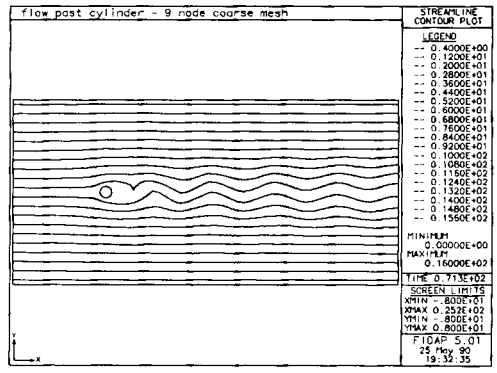

d) Coarse Mesh

Figure 16. Streamlines at t_{ref}

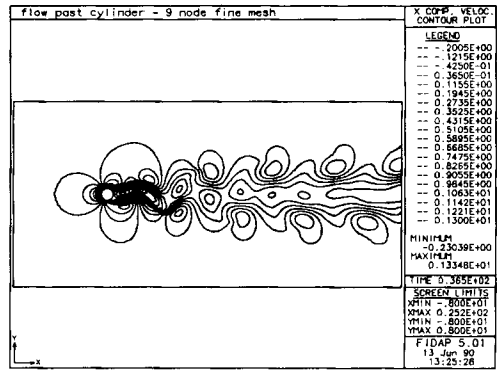

a) Fine Mesh

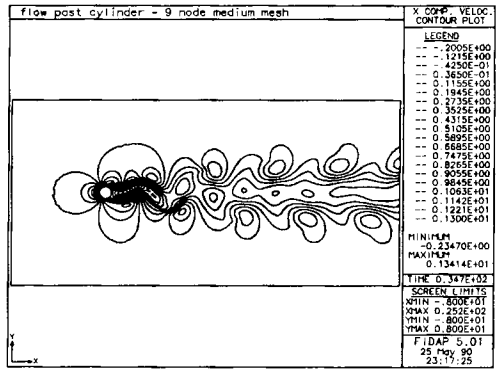

b) Medium Mesh

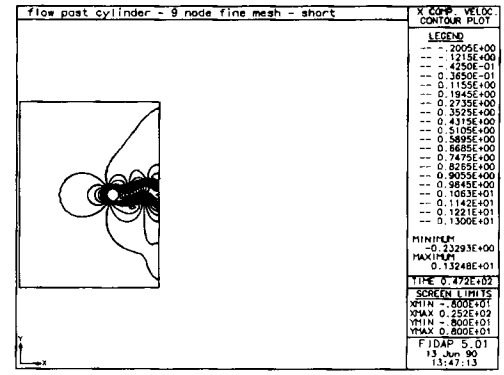

c) Short Mesh

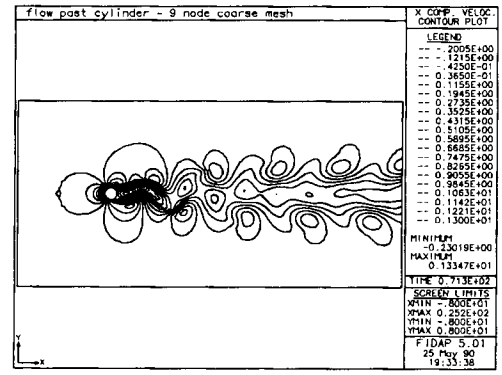

d) Coarse Mesh

Figure 17. u_x contour lines at t_{ref}

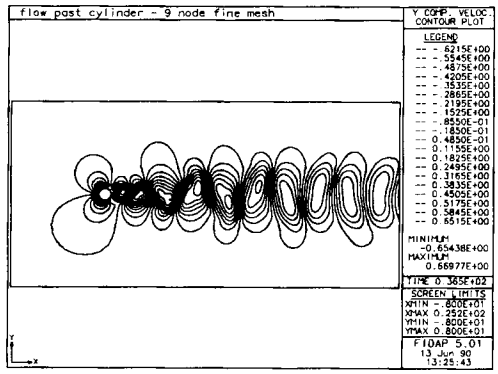

a) Fine Mesh

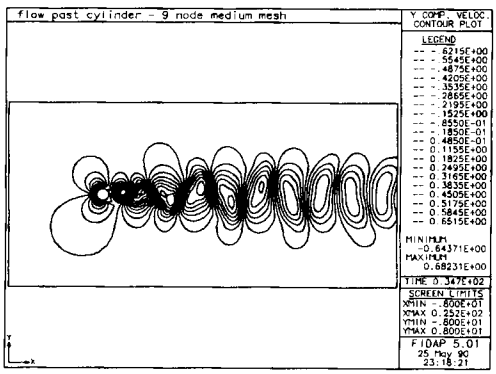

b) Medium Mesh

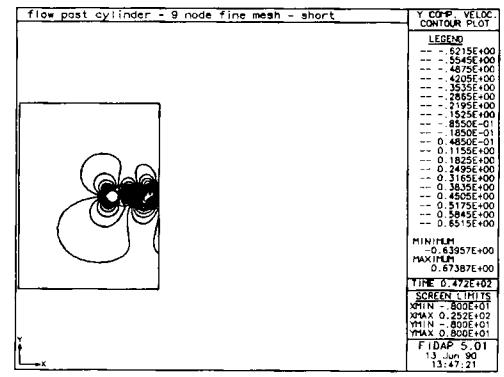

c) Short Mesh

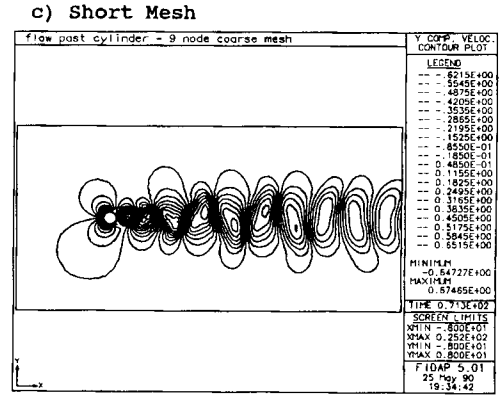

d) Coarse Mesh

Figure 18. u_y contour lines at t_{ref}

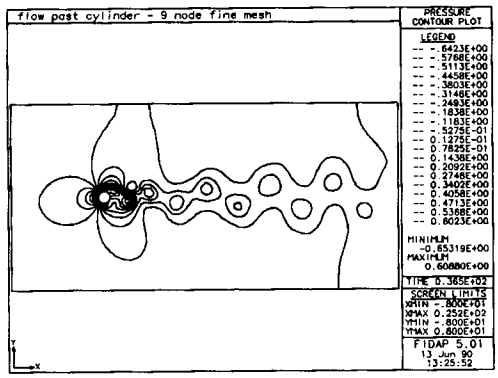

a) Fine Mesh

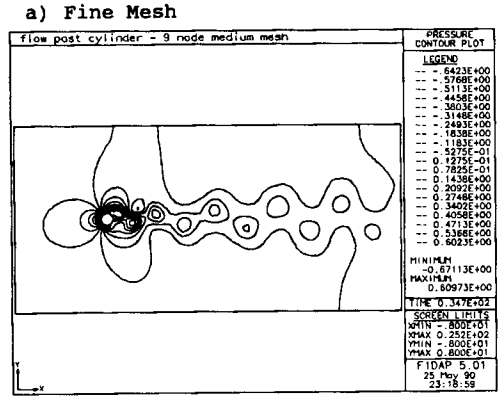

b) Medium Mesh

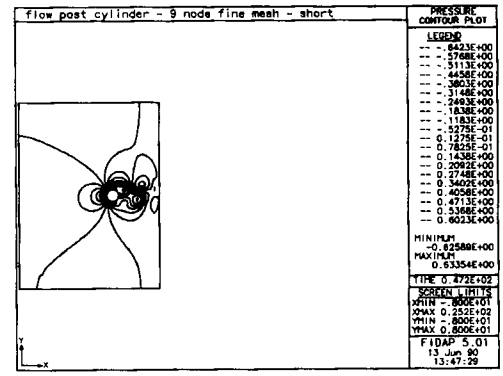

c) Short Mesh

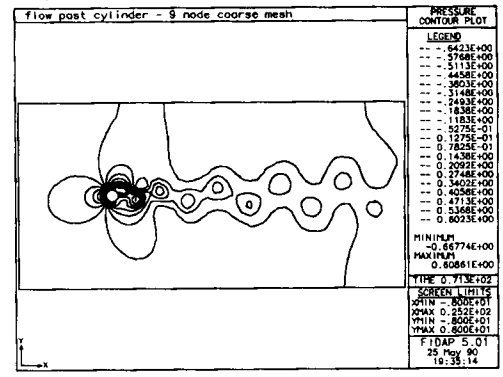

d) Coarse Mesh

Figure 19. Pressure distribution at t_{ref}

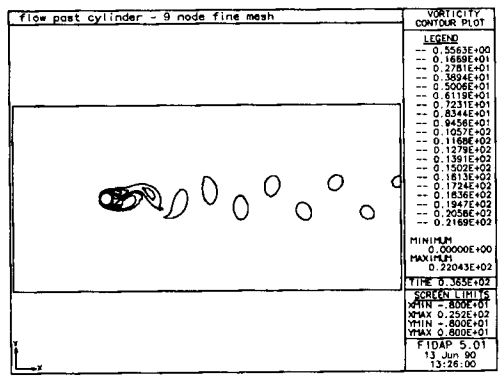

a) Fine Mesh

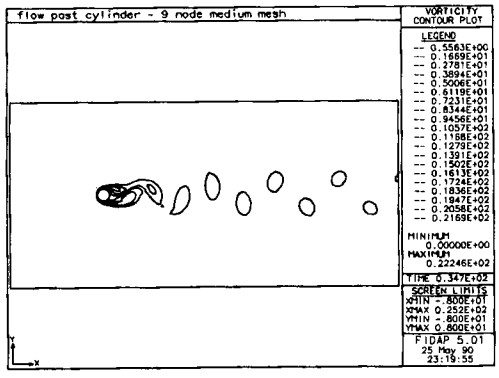

b) Medium Mesh

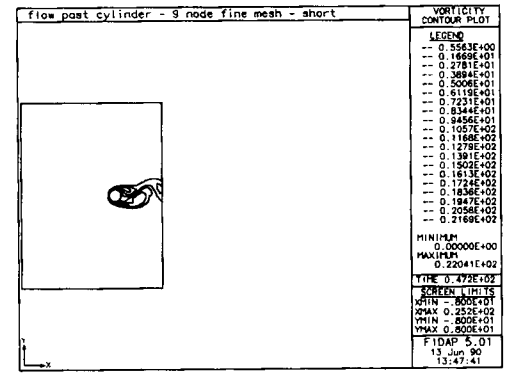

c) Short Mesh

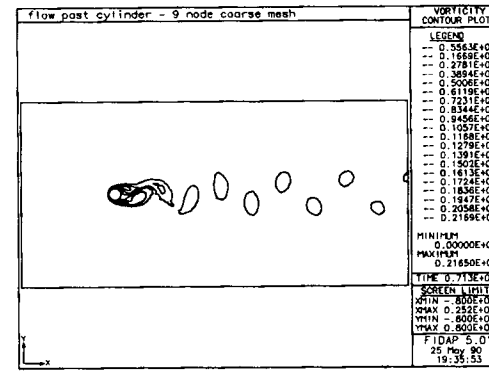

d) Coarse Mesh

Figure 20. Vorticity distribution at t_{ref}

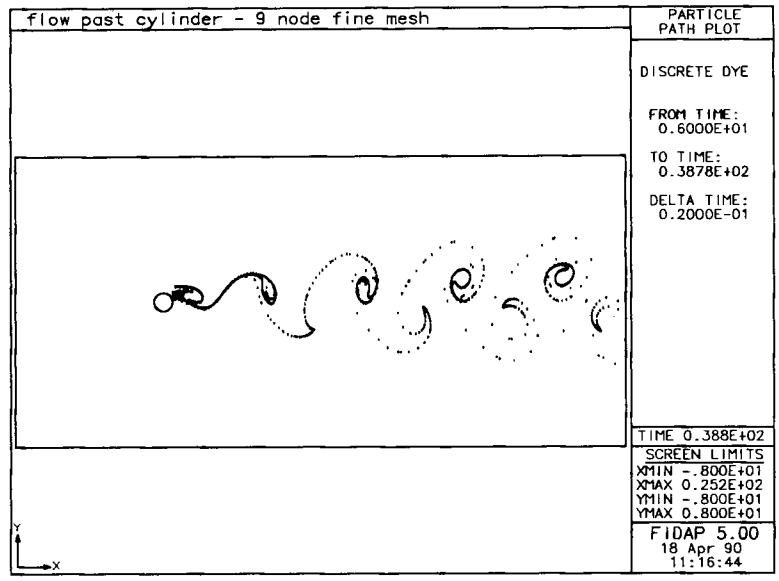

Figure 21. Discrete dye path plot of the vortex shedding at t_{ref}

Table II. Summary of vortex-shedding results

Mesh	Period τ	Strouhal no. $D/\tau V$	Wavelength λ	Vortex speed λ/τ	Average drag coefficient	Peak-to-peak drag	Peak-to-peak lift
Coarse	5·83	0·172	5·43	0·926	1·405	0·0215	0·7267
Medium	5·81	0·172	5·31	0·912	1·410	0·0205	0·7267
Fine	5·80	0·173	5·32	0·915	1·411	0·0203	0·7267
Short	6·21	0·161	—	—	1·384	0·0270	0·7200

A number of other quantities are of particular interest for the vortex-shedding problem. These include the period τ for one shedding cycle (during which two vortices are shed, one from the top and one from the bottom), the Strouhal number $St = Df/V$ (where $f = 1/\tau$ is the shedding frequency), the wavelength λ, the vortex speed (λ/τ), the average and peak-to-peak values of the drag coefficient C_D and the peak-to-peak value of the lift coefficient C_L. These quantities were determined from visual examination of the various time history plots and are summarized in Table II for each mesh.

DISCUSSION

Visually, the results from the fine mesh are identical to those for the medium mesh, while the numerical results in Table II show less than a 0·3% variation in any quantity. Thus it is reasonable to conclude that the results on the fine mesh are essentially grid-converged. Although it would be desirable to use Richardson extrapolation to further verify grid convergence, the non-regular nature of the mesh employed as well as the variable-time-increment time integration technique used preclude such an analysis.

The natural boundary condition employed in this study effectively sets a pressure level of zero at the outflow. This is clearly seen when comparing the plots of quantities at the $x=4$ location for the fine and short meshes. A fascinating result of this study is the qualitative agreement of the results on the fine and short meshes despite the significant difference in the various quantities at $x=4$ for these meshes. Although the quantitative comparison of the various results does show the shortcomings of the truncated computational domain, the fact that vortex shedding still occurs shows the effectiveness of the natural boundary condition that arises from the application of the finite element method.

A disturbing feature of the results on the short mesh is the 'noisy' nature of many of the computed quantities at the outflow boundary ($x=4$) of this mesh. The source of this noise is not clear, although it is our belief that it is related to effects associated with the premature termination of the computational domain.

REFERENCES

1. M. S. Engelman, FIDAP *Theoretical Manual, Version 5.0*, Fluid Dynamics International, Evanston, IL, 1990.
2. M. S. Engelman, R. L. Sani, P.M. Gresho and M. Bercovier, 'Consistent vs. reduced quadrature penalty methods for incompressible media using several old and new elements', *Int. j. numer. methods fluids*, **2**, 25 (1984).
3. P. M. Gresho, R. L. Lee and R. L. Sani, 'On the time dependent solution of the incompressible Navier–Stokes equations in two and three dimensions', *Recent Advances in Numerical Methods in Fluids*, Pineridge Press, Swansea, 1980.
4. M. S. Engelman, G. Strang and K. J. Bathe, 'The application of quasi-Newton methods in fluid mechanics', *Int. j. numer. methods eng.*, **17**, 707 (1981).
5. I. Hasbani and M. Engelman, 'Out of core solution of linear equations with non-symmetric coefficient matrix', *Comput. Fluids*, **7**, 13 (1979).
6. P. M. Gresho, S. T. Chan, R. L. Lee and C. D. Upson, 'A modified finite element method for solving the time-dependent incompressible Navier–Stokes equations. Part 2: Applications', *Int. j. numer. methods fluids*, **4**, 619–640 (1984).
7. A Brooks and T. Hughes, 'Streamline upwind/Petrov Galerkin formulation for convection-dominated flows with particular emphasis on the incompressible Navier–Stokes equations', *Comput. Methods Appl. Mech. Eng.*, **32**, 199 (1982).